

Detector-based prediction of dose and positron-emitting isotope profiles in particle therapy using a deep learning approach

Atiq Ur Rahman, Mythra Varun Nemallapudi[‡],
Cheng-Ying Chou, Shih-Chang Lee, Chih-Hsun Lin

Atiq Ur Rahman is from National Central University, Taiwan

M. V. Nemallapudi, Shih-Chang Lee, Chih-Hsun Lin are with the Academia Sinica, Taiwan

Cheng-Ying Chou is with National Taiwan University, Taiwan

E-mail: mythravarun01@gmail.com

01 April 2022

Abstract. Estimating the real dose distribution during proton therapy through experimental measurements is key to optimizing treatment planning and ensuring treatment quality. Positron emission correlates with dose distribution, but this correlation is non-linear and difficult to estimate in practical situations. We propose a deep learning-based method that utilizes raw coincidence data from readouts of palm-sized PET modules and predicts the positron activity and dose distributions bypassing traditional reconstruction steps. An extensive simulation dataset was generated using the GATE/Geant4 10.4 toolkit and a human CT phantom with a compact in-beam PET imaging setup for realistic single-fraction dose delivery. Conditional generative adversarial networks were trained to generate dose maps conditioned to the coincidence distributions on the detector. The generated dose maps are used to validate the range against simulated output. We evaluated the model performance through mean relative error (MRE), absolute dose fraction difference, and shift in Bragg peak position, and present it as a function of the detector threshold, the number of coincidences required, and other conditions that optimize the predictive power of the model. The results show that the model can predict the Bragg peak position and dose for mono-energetic irradiation between 50 MeV and 122 MeV with uncertainties less than 1% and 2%, respectively, with 10^5 coincidences acquired for five minutes post-irradiation. An important aspect of this simulation study is the use of compact detectors applicable in a treatment scenario, which operate on very low counts and the demonstration of a method for direct reconstruction. Through our analysis, we can continue to expand the scope of inverse modeling to simulate realistic data by learning imaging and experimental physics in radiation therapy from observations.

Keywords: Proton therapy, direct reconstruction, positron emitter, range verification, dose verification, conditional GAN, in-beam PET

1. Introduction

Fast, precise, and physically optimal in-vivo monitoring for dose and range verification during proton therapy is a challenging and critical task that can enhance the scope of treatment planning. There are two main methods to perform dose and range verification. The first method requires a measurement

of the primary or secondary protons using some invasive implant devices or directly measuring the high-energy proton beam exiting from the tumor (Lu 2008, Watts et al. 2009). The scope of the invasive method is limited because it demands implanting a dosimeter in the radiological path in the tumor region. Methods involving direct proton beam measurements require high-energy proton beams >250 MeV for deep tumor regions, such as the pelvis. Such methods only provide the range shift within the patient without full knowledge of the tumor area. In the second method for dose and range verification, the secondary particles generated during the proton beam irradiation provide the necessary information. As a proton beam passes through the tissue, positron annihilated gamma (PAG), and prompt gamma (PG) emitting isotopes are produced due to the inelastic nuclear interaction of protons, and their energy-dependent distribution is correlated to the depth dose profile (Parodi 2000, Min et al. 2006) with a systematic lag (Paganetti 2012, Parodi et al. 2007). Precise activity measurement through PET (Paans & Schippers 1993) experiences several challenges such as photon attenuation, detector efficiency, uncertainties introduced by non-linearity of the positron range, and random and scattered events inside the detector (Vaquero & Kinahan 2015). For PET image reconstruction, analytical and iterative reconstructions are the main conventional reconstruction techniques. The analytical reconstruction technique is based on the non-stochastic conjecture and attempts to estimate the image using completely deterministic mathematical solutions (Alessio et al. 2005). Analytical reconstruction ignores the noise contributions, while iterative methods can incorporate the noise effects because the updating step during each iteration can potentially make the final estimation better than the previous ones (Tong et al. 2010). But the iterative reconstruction method needs an accurate and fast estimation of the system response matrix (SRM), which should include components such as geometry, noise effects, and local variations like channel detection efficiency variation of the readouts. The simulation and integration of all components of SRM make it a large-scale, complex, and computationally intensive task (Iriarte et al. 2016). Mapping the reconstructed activity profiles to dose distributions can be complicated in real patient treatment because the activation of the positron emitters is due to inelastic nuclear interactions, while the proton loses the energy mainly due to the electromagnetic interactions (Paganetti & El Fakhri 2015). Two main approaches have been proposed as a solution to verify the dose. The first is an indirect approach to verify the dose activity profile of the positron emitters. One of such methods (Enghardt et al. 2004, Fiedler et al. 2010) is an interactive solution based on a direct comparison between the simulated and measured signals of β^+ superimposed on the CT image. If there is a mismatch between the positions of the two contours, a possible cause of the deviation is speculated, and the PET signal is recalculated after modifications are made to the treatment planning system. Although the indirect method is satisfactory in accuracy and easy to implement, it cannot directly estimate the difference between delivered and planned doses. The second method is the direct method, in which the dose is plotted from the activity profile of the positron emitter. One such attempt (Fourkal et al. 2009) was proposed, which implemented an analytical model for estimating dose from three-dimensional information preserved in PET signals. The estimated kernel called the positron emitter species matrix (PESM) deconvolved with the reconstructed positron activity, which estimates that the difference between predicted and delivered doses is within 2%. Other proposed methods were analytical methods based on modeling functions applied to reconstructed PET activity profiles and have better accuracy than the interactive methods (Parodi & Bortfeld 2006, Attanasi et al. 2011, Remmele et al. 2011) when evaluating homogeneous phantoms. A pioneering statistical approach that (Masuda et al. 2019) applies maximum likelihood estimation method (MLEM) combined with the filtering to obtain 2D dose profiles showed promising results under statistical noise, with relative errors of mono-energetic and spread-out Bragg peaks

(SOBP) in the range of 10% or less. SOBP. A study (Liu et al. 2019) based on deep learning developed recurrent neural networks (RNN) that are trained on simulated depth distributions of ^{11}C and ^{15}O to obtain dose maps. However, the (Liu et al. 2019) study was based on the intrinsic isotopic distributions that cannot be measured and hence cannot be verified experimentally. The second sequence of the RNN model-based study combined the PET detector model, proton beam stopping power, and anatomical information using the reconstructed dose-mapping profile (Hu et al. 2020). Another study (Zhang et al. 2021) used deep learning methods to predict proton dose in 3D. The study was performed on a ring-shaped PET prototype with 88,000 crystal elements to reconstruct PET activity using single slice re-binning reconstruction and 2D OSEM iterative reconstruction algorithms. The above described PET signal-based dose mapping solutions directly or indirectly rely on the activity profiles reconstructed by using conventional reconstruction methods. It is desirable to map the dose distributions directly from the detector data without performing traditional reconstruction, and a neural network can be trained on the detector-induced uncertainties. Previously, a deep learning-based solution named DeepPET using an encoder-decoder model was proposed for diagnostic PET systems, which directly transferred the sinogram data into the activity space after training with high-quality real data. It delivered better image quality than the traditional optimized image reconstruction method (Häggström et al. 2019). Another deep learning-based direct reconstruction study was conducted (Ronneberger & Fischer 2015), which showed robustness and accuracy compared to conventional reconstruction methods. Deep learning can be introduced in the dose reconstruction problem after conventional reconstruction of PET activity distribution. This approach is a deep learning-based post-reconstruction filtering to obtain dose maps that still rely on regular reconstruction, as implemented in Hu *et al.* However, direct proton dose mapping from raw detector data has not yet been explored. In our work, we propose a deep learning framework to directly map the detector data into the corresponding dose distribution without reconstructing the PET activity distribution. The same approach can also be used to directly reconstruct the activity profiles of the isotopes by using the 2D raw coincidence projection data as input information. Previous solutions for in-vivo dose monitoring utilized large PET scanners and heavy PG detectors. Our study aims to develop the neural network to be useful for compact PET detectors of the kind described in (Nemallapudi et al. 2021, Su et al. 2020, Ozoemelum et al. 2020), which are ideal for practical application in the highly restrictive treatment environment while also facing the challenges of low count rates. Our study’s motivation for using a small detector was to examine the possibility of using a miniature imaging solution combined with the feature extraction capabilities of deep networks as an in vivo monitoring solution. A quantitative study was also conducted to estimate the average number of detector counts required to achieve acceptable accuracy using a palm-sized detector prototype.

The state-of-the-art deep generative models are variant autoencoder (VAE) and GAN models, used extensively for image synthesis problems (Oussidi & Elhassouny 2018). GAN models are superior to VAEs because of their ability to extract features from complex data and generate high-quality images. GANs are a good choice because of their excellent ability to learn domain-dependent and domain-independent features. In our study, we used a deep generative model originally proposed by (Mirza & Osindero 2014) as conditional GANs network and firstly implemented in image to image translation problem (Isola et al. 2017). Zhang *et al.*, also applied the disocGAN variant of generative adversarial networks (GAN), which is close to the model used in our research. However, there are significant differences between our study and their disocGAN-based study. We used only 1,024 detector crystal elements and raw coincidence detector data without image reconstruction algorithms or filters. Our work is supervised learning, which requires labeled pairs of source and target images

as training data. In generative models, once the generator and the discriminator are alternately trained, the trained generator model is obtained and used as an independent model for prediction. In our work, dose maps can be obtained as the output by importing 2D coincidence projection data into the model. By applying this model, we can learn the underlying imaging physics, detector geometry, and detector non-uniformity directly from experimental data.

2. Materials and methods

2.1. Simulation setup for proton beam irradiation

We used the Geant4 based simulation framework GATE (Jan et al. 2011, Grevillot et al. 2011) to generate Monte Carlo simulation data for a realistic proton therapy setup. Irradiation of a pencil beam source on an abdominal CT phantom was used for data generation. The phantom dimensions are 302 mm×302 mm×180.5 mm with the spatial resolution of 0.589 mm×0.589 mm× 0.500 mm.

The HU range of the phantom was divided into 24 bins according to the scheme described in (Schneider et al. 2000) and details are summarized in Table 1. The beam propagates along the z axis, and the beam profile was assumed to be a Gaussian distribution with standard deviations σ_x and σ_y at the iso-center position. We have performed simulations for five different spot sizes with standard deviations ranging from 3 to 5 mm with an interval of 0.5 mm in both x and y dimensions. A total of 150 million protons were used as primary particles with a Gaussian energy spectrum with a standard deviation of 1% from the target proton energy. The phantom was irradiated at 10 different positions on the DICOM image with beam energy from 50 to 122 MeV in 4 MeV intervals. The distance between the simulated beam origin and the face of the phantom center is kept at 50 cm. The physics list QSP_BIC_HP_EMZ was employed in our study as it showed more accurate results over QSP_BIC_HP_EMY (Winterhalter et al. 2020). ^{10}C , ^{11}C , ^{13}N and ^{15}O have large production cross-sections. Among them, ^{11}C , and ^{15}O have relatively long lifetimes and larger production cross-sections, which are therefore the focus of our study. The depth dose distribution and the production information of positron-emitting isotopes ^{11}C and ^{15}O were stored in a voxelized image using the dose and production-stopping actor available in GATE. Dose and positron activity have been stored with a spatial resolution of 0.589 mm×0.352 mm×0.205 mm.

2.2. Detector simulation setup

A palm-sized dual-head PET has 8 modules. Each module has 64 monolithic LYSO crystals with dimensions of 3.2 mm×3.2 mm×20 mm and 0.2 mm spacing between each module, results in the detector size of 52 ×104 mm in the yz plane. The spacing between the dual-head PET modules is kept at 302 mm to accommodate the phantom between the modules. The detector has an energy resolution of 10% at 511 keV and a temporal resolution of 250 ps FWHM. The energy threshold was kept at 150 keV to reduce low energy counts and maintain an acceptable noise level similar to a realistic detector. The isotope activities of ^{11}C and ^{15}C are imported in the same model configuration that was used during proton beam irradiation as described in Sec. 2.1. Voxel-based production and stopping information of ^{11}C and ^{15}C were used to generate the coincidence data in the palm-sized PET setting. As we import the number of isotopes as an activity in GATE, the decay rate constant $\lambda_{^{11}\text{C}}$ and $\lambda_{^{15}\text{O}}$ of the corresponding isotope were considered to model ^{11}C and ^{15}O decay at in-beam PET environment. The positions of the isotopes are available at the level of a voxel, and the finer positions were simulated randomly within each voxel 0.2 mm. The production information of ^{11}C and ^{15}O was simulated as activity $A(\mathbf{r}, t)$ by preserving the relative isotopic distribution spatially

Table 1. Relative elemental composition and density of different materials in accordance to the range of Hounsfield Units (HU) (Schneider et al. 2000).

HU Range	(g cm ⁻³)	H	C	N	O	Na	Mg	P	S	Cl	K	Ca	Ar
[-1050,-950]	0.001290	0	0	75.6	23.2								1.3
[-950,-120]	0.880110	10.3	10.5	3.1	74.9	0.2		0.2	0.3	0.3	0.2		
[-120,-82]	0.926691	11.6	68.1	0.2	19.8	0.1			0.1	0.1			
[-82,-52]	0.957382	11.3	56.7	0.9	30.8	0.1			0.1	0.1			
[-52,-22]	0.984227	11.0	45.8	1.5	41.1	0.1		0.1	0.2	0.2			
[-22,7]	1.011170	10.8	35.6	22	50.9			0.1	0.2	0.2			
[7,18]	1.029550	10.6	28.4	2.6	57.8			0.1	0.2	0.2	0.1		
[18,80]	1.061601	10.3	13.4	3.0	72.3	0.2		0.2	0.2	0.2	0.2		
[80,120]	1.119903	9.4	20.7	6.2	62.2	0.6			0.6	0.3			
[120,200]	1.111150	9.5	45.5	2.5	35.5	0.1		2.1	0.1	0.1	0.1	4.5	
[200,300]	1.164774	8.9	42.3	2.7	36.3	0.1		3.0	0.1	0.1	0.1	6.4	
[300,400]	1.123741	8.2	39.1	2.9	37.2	0.1		3.9	0.1	0.1	0.1	8.3	
[400,500]	1.282950	7.6	36.1	3.0	38.0	0.1	0.1	4.7	0.2	0.1		10.1	
[500,600]	1.342190	7.1	33.5	3.2	38.7	0.1	0.1	5.4	0.2			11.7	
[600,700]	1.401421	6.6	31.0	3.3	39.4	0.1	0.1	6.1	0.2			13.2	
[700,800]	1.460663	6.1	28.7	3.5	40.0	0.1	0.1	6.7	0.2			14.6	
[800,900]	1.519900	5.6	26.5	3.6	40.5	0.1	0.2	7.3	0.3			15.9	
[900,1000]	1.579142	5.2	24.6	3.7	41.1	0.1	0.2	7.8	0.3			17.0	
[1000,1100]	1.638380	4.9	22.7	3.8	41.6	0.1	0.2	8.3				18.1	
[1100,1200]	1.697620	4.5	21.0	3.9	42.0	0.1	0.2	8.8	0.2			19.2	
[1200,1300]	1.756860	4.2	19.4	4.0	42.5	0.1	0.2	9.2	0.3			20.0	
[1300,1400]	1.816100	3.9	17.9	4.1	42.9	0.1	0.2	9.6	0.3			21.1	
[1400,1500]	1.875340	3.6	16.5	4.2	43.2	0.1	0.2	10.0	0.3			21.9	
[1600,5000]	1.946430	3.4	15.5	4.2	43.5	0.1	0.2	10.3	0.3			22.5	

inside the phantom. The resulting distribution in time approximates a realistic simulation limited to the two dominant isotopes. .

$$A(\mathbf{r}, t) = \lambda_{11\text{C}} \times N_{11\text{C}}(\mathbf{r}).\exp[-\lambda_{11\text{C}}.t] + \lambda_{15\text{O}} \times N_{15\text{O}}(\mathbf{r}).\exp[-\lambda_{15\text{O}}.t], \quad (1)$$

where $N_{11\text{C}}$ and $N_{15\text{O}}$ are numbers of isotopes of ^{11}C and ^{15}O produced during proton irradiation while $\lambda_{11\text{C}}$ and $\lambda_{15\text{O}}$ are decay constants of the respective isotopes. The coincidence data were recorded for 300 seconds, during which $\sim 81\%$ of ^{15}O and $\sim 15\%$ of ^{11}C would have decayed. In order to reduce simulation time and computational cost, we linearly scaled up the activity by a factor of 100 to reach the proton fluxes on the order of 10^{10} since the production of the positron emitters is proportional to proton fluxes. The proton fluxes needed to generate the coincidence data at 110 MeV with different detector thresholds for our palm-sized prototype with described simulation conditions at a distance of 302 mm are shown in Fig. 1(a). The recorded number of coincidences at a given proton flux varies with the proton energy when detector spacing is adjusted for different phantom sizes, as shown in Fig. 1(b).

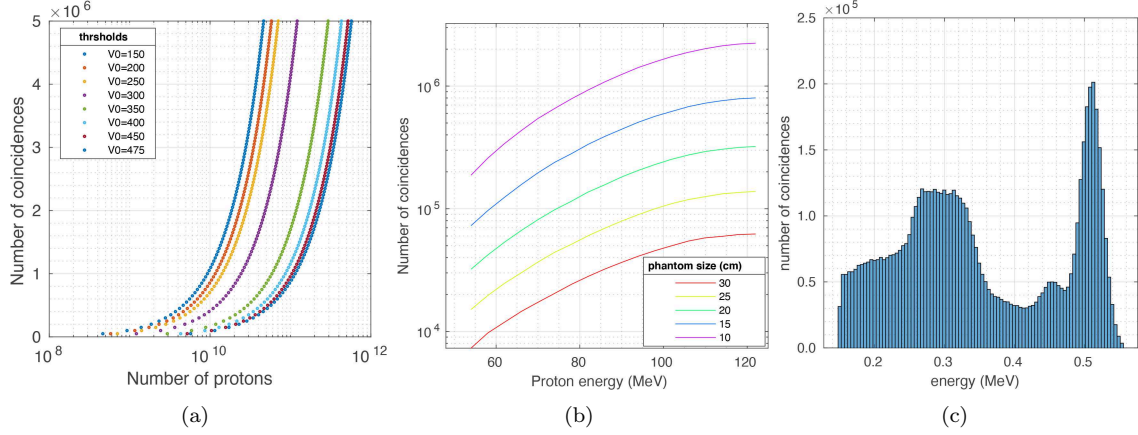


Figure 1. Results for our detector prototype. (a) Relation between the detected number of coincidences and number of protons under different detector threshold values. (b) Relation between detected number of coincidences for different proton energies (MeV) and human tissue phantom of different dimensions while changing the inter-detector spacing according to phantom dimension, and (c) simulated energy spectrum for the LYSO crystal.

2.3. Deep learning model

Generally, image mapping problems using measured data can be expressed as:

$$Y = HX, \quad (2)$$

where Y is the measurement data, H is the probability matrix, and X is the true data. The essence of our problem is pairwise image translation, where the target $X : \{x_i\}$ is in a different domain than the source $Y : \{y_i\}$ domain. In the context of our study, the X is the dose distribution, and Y represents the corresponding measured data, which is a coincidence map on the detectors. The cGAN model uses the conditional variant to initiate the training of the model. Conditional constraints can drive the model to converge to the expected results with significant performance stability. The objective of cGAN can be expressed as:

$$\begin{aligned} L_{cGANs}(D, G) &= \min_G \max_D U(D, G) \\ L_{cGANs}(D, G) &= E_{x \sim P_{data}(x)} [\log_2 D(x|y)] + E_{x \sim P_z(x)} [\log_2 (1 - D(G(z|y)))], \end{aligned} \quad (3)$$

where $G : \{y, z\} \rightarrow x$ is a joint representation of the generator part of the cGAN model. Meanwhile, D describes the discriminator part of the model, which computes the probability that the sample came from the training data instead of G . The source distribution is represented by $P_{data}(x)$, and the source distribution combined with random noise z is represented as $P_z(x)$. G strives to tune the parameters to minimize $\log_2(1 - D(G(z|y)))$, while D tunes the parameters to maximize discriminator loss. Training with adversarial loss improves image quality but does not guarantee similarity to the target image. To improve accuracy, L1 loss-based regularization R_{L1} is employed in the cGAN model. λ is the weight of the regularization. Post-regularization objective function is expressed as:

$$G^* = \arg \min_G \max_D L_{cGANs}(D, G) + \lambda R_{L1}, \quad (4)$$

Our deep learning model consists of a discriminator and a generator as two primary components where the output of the generator and discriminator both are conditioned on input.

2.3.1. The architecture of the conditional generative adversarial network This section will describe the implementation of the cGAN model to convert the coincidence map to a dose map. The model was implemented using the Nvidia GPU Generation GeForce RTX-3090 in the Keras deep learning framework. As described in Sec. 2.3, the model has two main working partners, the discriminator and the generator.

The effective receptive field (RF) based discriminator architecture consists of a special classifier named patchGAN implemented as a down-sampling convolution network. It makes a patch-based prediction to flag the real or fake image. It selects a typical size (70×70) pixels and sweeps it over the image to calculate the patch-based probability map of real or fake images instead of computing the whole image at once. Two types of inputs are fed into the discriminator $X : \{x_i\}$ real and $\hat{X} : \{\hat{x}_i\}$ generated by the generator and the patch-based probability distribution for both images is calculated. For model optimization, we have applied the binary cross-entropy (BCE) as the loss function, which is further used by the model to estimate the penalties in the back-propagation step.

Table 2. A summary of the hyperparameters of the discriminator.

No.	Parameter	Value
1	Alpha for leakyReLU	0.2
2	Learning rate	0.0002
3	Loss weight	1
4	Activation function	Sigmoid
5	Loss function	Binary cross entropy
6	Optimization algorithm	Adaptive moment estimation (ADAM)
7	Beta parameter of (ADAM)	0.5

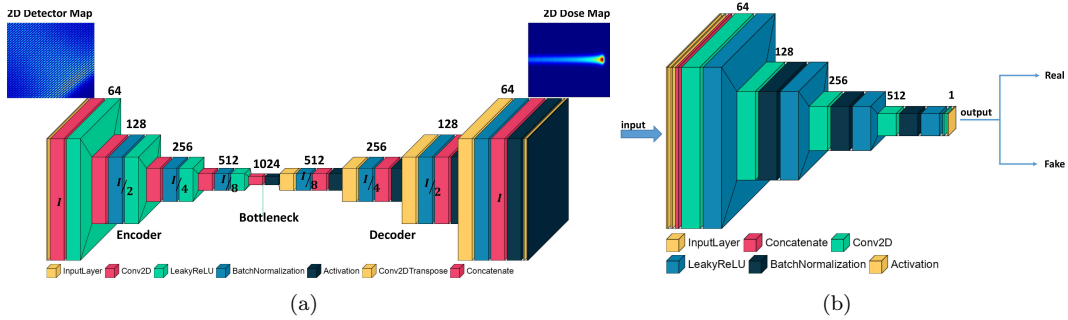


Figure 2. (a) Block diagrams of the generator(U-net), (b) Block diagram of the discriminator.

The generator part of our model has two symmetric encoder and decoder parts. As shown in Fig. 2(a), the encoder part downsamples the input image until the bottleneck, while the decoder part performs upsampling. Each encoder and decoder section consists of four blocks. Each normalization

block has convolution, pooling, batch normalization, dropout, and activation functions. Feature information may be lost during downsampling and passed to upsampling using connected layers. Connections are represented by assigning the same color codes to layers in Fig. 2(a). The upsampled final image has the same size as the input image. The implementation of the encoder and decoder is performed using unified encoder and decoder functions, which, in turn, build a layer block. The model converges to the final value with the scaling up of the kernels and layers, but it becomes a computationally expensive task.

We have used the tanh function as the activation function at the end of the downsampling, which predicts the generator output in the range of $[-1, 1]$. The generator training is performed with two loss functions. One is the discriminator loss while the other is L_1 which describes the mean absolute error (MAE) between the generated and actual distributions. Since the total loss function of the generator is a linear combination of the discriminator loss and the MAE loss, the weights of the two loss functions are kept at 0.01 and 1. The higher weight of the MAE loss enforces the generator to produce more plausible distributions instead of producing random images in the target domain. The GAN image translation model encourages keeping the generator stronger than the discriminator. This goal of convergence to the generated images close to the target images is accomplished by defining a double-component standalone model of the generator and discriminator, where the generator is on top of the discriminator.

A batch from the real coincidence-dose pair is first used for every training step to update the discriminator. Then a batch of images generated by the generator is used to update the discriminator, and the discriminator is updated with both real and fake maps. The generator is fed by the actual 2D coincidence map at the second training phase to predict the dose distribution. This generated dose map by the generator and the corresponding actual dose map of the corresponding input coincidence map is used to evaluate the loss function on the basis of every single image in the batch and update the generator's weights. The model is stored after every single epoch for invigilation of the performance. The optimized values of the hyperparameters for the generator and training sets are given in Table 3.

Table 3. A summary of hyperparameters for the generator.

No.	Parameter	Value
1	Alpha for leakyReLU	0.2
2	Loss function (L_1)	MAE
3	Loss weight (w_1)	1 (BCE)
4	Loss weight (w_2)	100 (MAE)
5	Activation function	tanh
6	Learning rate	0.0002
7	Batch size	2
8	Epochs	100
9	Optimization algorithm	Adaptive moment estimation (ADAM)
10	Beta parameter of (ADAM)	0.57

2.4. Training data preparation scheme

In the simulation, the two detector heads of the dual-head PET prototype are tagged as planes 0 and 1. The geometric layout of each detecting plane is comprised of modules numbered from 0 to 7. The default arrangement of the crystals in each module is designated from 0 to 63 for plane 0 of the prototype in Fig. 3(a). A unique crystal index is generated for each module channel from 0 to 511. A corresponding map of size 512×512 is populated by counting the number of coincidence pairs detected along the column for each crystal in plane 0 and each crystal in plane 1. A typical 2D coincidence map is shown in Fig. 3(b). We employed both direct coincidence and cross-coincidence to make our data representation similar to the Michelograms (Fahey 2002) originally used for 3D PET image reconstruction.

After obtaining all coincidence maps and the corresponding dose maps, we combined them into the paired source and target images, as shown in Fig. 2(a). Two datasets were generated. The first dataset consists of coincidence maps and corresponding dose maps as 2D image pairs for different detector thresholds. For the second dataset, the data containing the coincidence map and the corresponding dose map as 2D image pairs have three channels. Three-channel 2D coincidence maps were prepared by filtering coincidences in the three energy windows. The three maps are stacked as three channels of a 2D map. In the remainder of this paper, the three-channel coincidence map and the corresponding dose-paired dataset are designated as the three energy window (EW3) dataset. The energy windows are: a) 150 keV to 250 keV, b) 250 keV to 475 keV and c) >474 keV. We irradiated 10 locations at 18 energy levels using 5 different spot sizes and generated 900 corresponding image data. We split the total data into training data (63%), test data (21%) for model evaluation, and validation data (16%) for hyperparameter tuning.

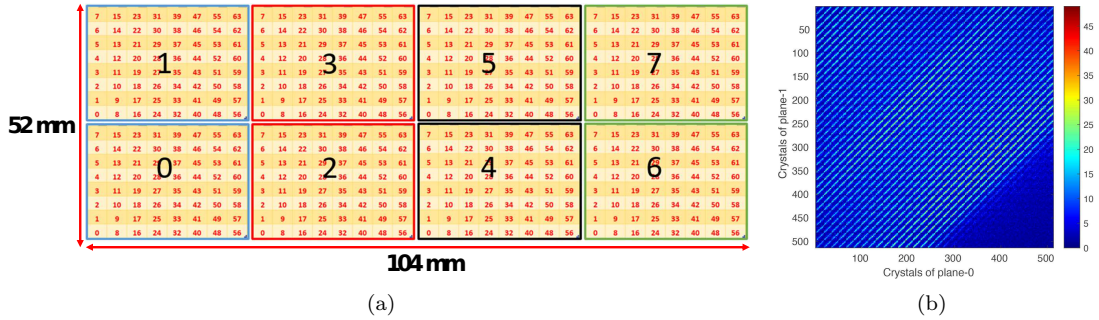


Figure 3. (a) Denotes arrangement of module and crystals in one plane, (b) shows 2D map for coincidences, (c) shows one typical 2D coincidences map for 110 MeV proton beam.

2.5. Model evaluation metrics

To evaluate the prediction of Bragg's peak position, we used the shift in the BP values of the predicted profile and the true profile. The 2D profiles were converted into 1D profiles, and then the 5% maximum values around the peak position of the true and predicted profiles were fitted to a Gaussian fit function. The ground truth values are known in simulation-based studies, allowing learning-based methods to quantify performance evaluations. We selected three variables as our model evaluation metrics. These metric variables are the mean relative error (MRE), the fractional

absolute dose error (δD), and the fractional shift of the Bragg peak (BP) denoted by (δR). We evaluated MRE and δD at two regions of interest (ROIs). The first region of interest, called ROI₁, consists of the entire beam profile region, while the second region of interest, ROI₂ contains the region enclosed between the 50% peak values on the proximal and the distal side of the Bragg peak. The MRE and δD are relevant variables to grade the predicted feature intensity, which is related to dose verification in the final image. The metrics are defined as:

$$\text{MRE} = \frac{1}{n} \sum_i^n \frac{|\hat{s}_i - s_i|}{\max(s)}, \quad (5)$$

where \hat{s}_i and s_i respectively represent the predicted and true values in a pixel in an ROI and n represents the total number of pixels within. In the MRE formula, $\max(s)$ represents the peak value of the true profile. The fractional absolute dose error is defined as:

$$\delta D = \frac{\left| \int_{-z_d}^{+z_d} \hat{\mathbf{D}}(z) dz - \int_{-z_d}^{+z_d} \mathbf{D}(z) dz \right|}{\int_{-z_d}^{+z_d} \mathbf{D}(z) dz}, \quad (6)$$

where $\hat{\mathbf{D}}$ denotes the 1D projection of the predicted dose profile, while \mathbf{D} denotes the true 1D projection of the dose profile from the simulation used as the ground truth. Here $-z_d$ denotes the position of the dose profile on the left of the BP, while the $+z_d$ denotes the dose position to the right of the BP. The shift in BP assesses the performance using a geometric feature related to range verification.

$$\delta R = \frac{\hat{R}_{BP} - R_{BP}}{R_{BP}}. \quad (7)$$

Here, \hat{R}_{BP} shows the BP position of the predicted profile, and R_{BP} shows the BP position of the true profile. We have used the fractional shift in BP for our results, where we divide the difference into two peaks with the BP position of the actual profile.

3. Results

3.1. Prediction of dose and positron-emitting isotope distribution

3.1.1. Prediction of dose and profile of β^+ emitting isotopes The results of dose prediction and mapping of positron-emitting isotopes are shown in this section. The key is to consider that the results of dose mapping and positron-emitting isotope mapping correspond to two independently trained models, one for dose prediction and the other for isotope distribution prediction. The first part of this section shows the general predictive capability of the dose. Fig. 4(a)-(c) shows the predicted dose map, the true dose map, and the absolute difference between the prediction and true values at 110 MeV energy in the test dataset. In each plot, the horizontal axis represents the longitudinal depth (z -axis) along the beam irradiation direction, and the vertical axis represents the transverse depth (y -axis) perpendicular to the beam direction. The predicted profile in Fig. 4(a) agrees well with the ground truth in Fig. 4(b). To gain more insight, the values of the pixels along the y -axis are summed to obtain the 1D dose distribution as a function of longitudinal depth. Fig. 4(h) shows that the discrepancy between the true and predicted BP locations is about 0.35 mm, less than 1% of the BP peak position, and an absolute dose uncertainty of less than 2%. Similarly, pixel values

along the longitudinal depth are summed to obtain the transverse profile of the dose in Fig. 4(j). The general prediction capability of the positron-emitting isotopes can be observed in Fig. 4(d)-(f). The integrated depth profile of the positron-emitting isotopes of ^{11}C and ^{15}O was predicted using an AI-based model taking detector coincidence data as input for prediction. The image size remains the same as the dimension of the detector plane. The absolute difference in positron activity is predicted to be within $\pm 2\%$ uncertainty, while the shift in BP was predicted to be ± 0.5 mm, constituting less than 1.3% of the longitudinal depth. 1D profiles of positron emitters can be seen in Fig. 4(i) and Fig. 4(k). This section shows the evaluation of the model on the test data using the mean of the post-training metric variables MRE, δD , and δR . MRE, fractional dose shift, and fractional shift in BP for complete test data were calculated from the histograms in Fig. 5(a)-(c). The results with the corresponding error bars are described in Table 4. The results are then presented within 95% confidence intervals.

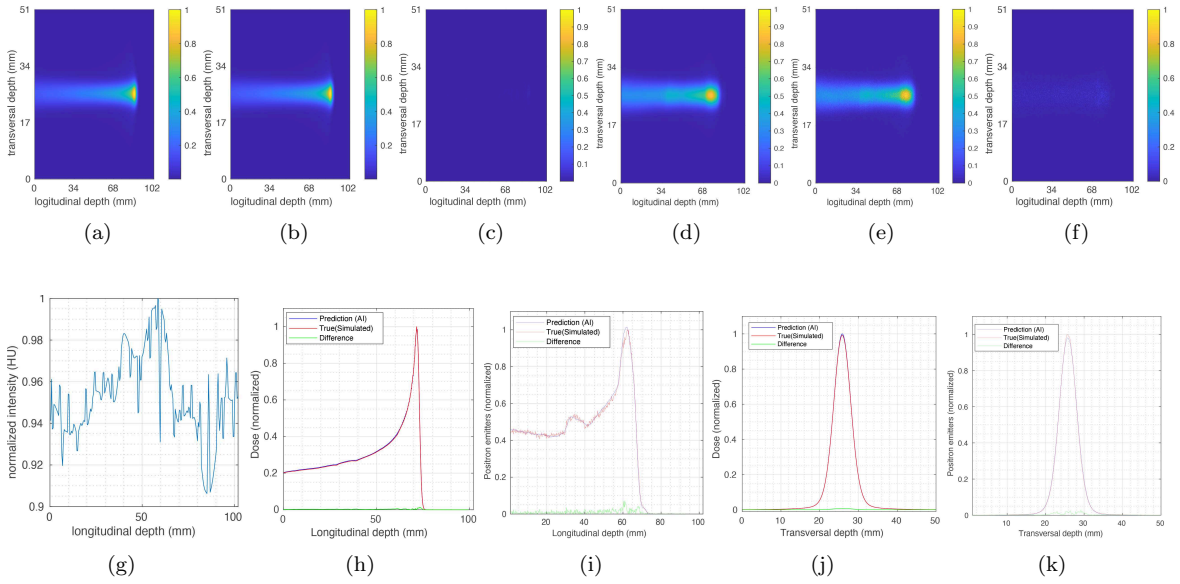


Figure 4. (a) shows the generated dose profile using the AI model, (b) shows the true simulated dose profile, (c) shows the absolute difference in the generated and true dose profiles, (d) shows the generated β^+ profile using the AI model, (e) shows the true simulated profile of β^+ , (f) shows the absolute difference in the generated and true β^+ profiles, (g) shows the material density normalized to peak of Hounsfield units obtained as 1D projection of averaged slice of 3D phantom, (h) shows the 1D dose profile normalized to the peak position of the target, (i) shows the 1D β^+ profile normalized to the peak position of the target, (j) shows the 1D dose profile of in transversal depth, and (k) shows the 1D profile of positron-emitting isotopes in transversal depth. Blu, red, and green curves represent the AI prediction, the true profile, and the difference between the predicted and true values, respectively.

3.2. Performance evaluation

During model training, we saved the trained model at each epoch to see how the model converged on the metric variables MRE, δD , and δR . To obtain reasonably unbiased estimates, we examined

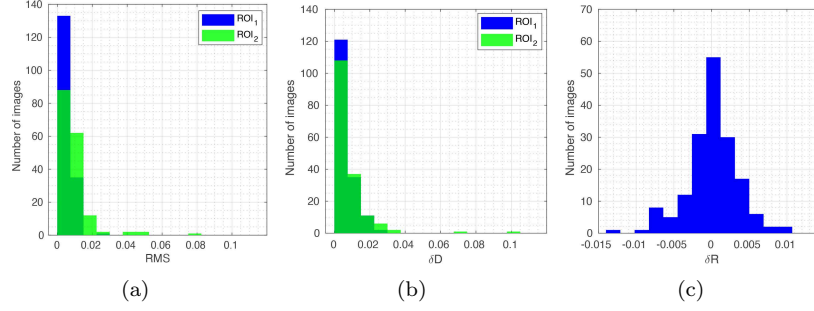


Figure 5. (a) Histogram of the MRE for test dataset, (b) Histogram of absolute fractional dose differences (δD) for complete test dataset in ROI₁ and ROI₂, (c) shows the fractional shift in the BP (δR) for the complete test dataset.

the model performance on the test dataset after each epoch to estimate the stable phase of the model for up to 1200 epochs. The stable values of the quality variables were derived from the 1D histograms for each epoch shown in Fig. 6. The mean value of the histograms for each metric variable represents the model's performance at that specific epoch. Considerable convergence can be seen after 250 epochs for MRE, δD , and δR . The baseline prediction value of MRE is less than 2%, as shown in Fig. 6(a), and the error in δD drops up to 3% shown in Fig. 6(b) while the shift in BP is observed within $\pm 0.5\%$ as shown in Fig. 6(c) after 250 epochs. The uncertainty of the prediction in ROI₁ is smaller than ROI₂ at all epochs for the three metric variables.

Table 4. Summary of metrics for the test dataset.

	MRE	δD	$\delta R(\%)$
ROI ₁	0.0156 ± 0.0098	0.014 ± 0.012	± 1.36
ROI ₂	0.0167 ± 0.00102	0.021 ± 0.015	

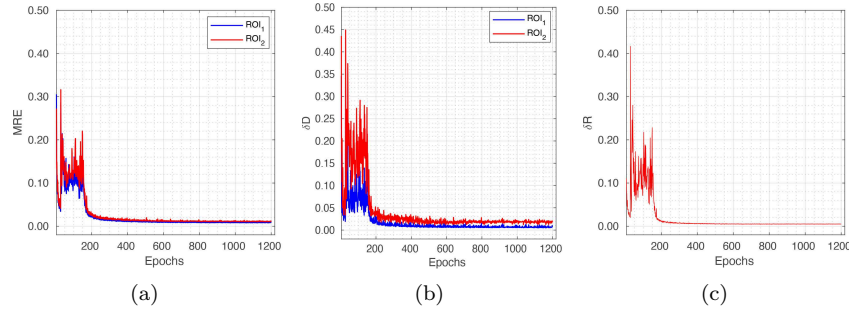


Figure 6. (a) shows the MRE as a function of epochs in ROI₁ and ROI₂ for the test dataset, (b) shows the absolute fractional dose difference as a function of epochs in ROI₁ and ROI₂ for the test dataset, (c) shows the absolute fractional shift of BP as a function of epochs.

3.3. Count-based analysis

The AI model was tested for a number of coincidence data to estimate the minimum number of coincidences on average for predicting dose and BP shift. The coincidence counts range from 7.3×10^3 to 8×10^4 for the 30 cm phantom case with the palm-sized detector described in Sec. 2.2 with a scan time of 300 seconds shown in Fig. 1(b). To check the model performance with different numbers of coincidence events, we have performed training using approximately 10 times more coincidence data. Fig. 7 compares the accuracy of the model as a function of coincidence data. The number of coincidences detected in our palm-sized prototype detector can be improved by increasing the proton dose shown in Fig. 1(a). In the count-based analysis, we calculated the average minimum number of coincidences for MRE, fractional dose, and fractional shift in BP only using photopeak data with a dataset of threshold 475 keV as shown in Fig. 7(a)-(c). It is worth noting that our photopeak map data range from 2×10^3 to 1.48×10^5 counts in a total of 74 bins with an increase of 2.0×10^3 . Table 5 summarizes the number of coincidences required for the prediction uncertainty of ROI₁ and ROI₂ to be lower than 4%, 3%, 2%, and 1%. Analysis for average coincidence was performed for only one threshold corresponding to the photopeak coincidences because preparing a complete test dataset of coincidence maps for all threshold values and energies requires an extensively large disk space and analysis time. But we have shown the model performance for 90 MeV proton beam as a function of the coincidences and important threshold conditions, as shown in Fig. 7(d)-(e).

Table 5. A summary of the count-based study showing the number of photo-peak coincidences needed to achieve the level of uncertainty for MRE, δD , and δR .

Quantity	uncertainty	No. of photo peak coincidences	
		ROI ₁	ROI ₂
MRE	4%	5660	6322
	3%	7019	8725
	2%	11143	25158
δD	4%	23387	23387
	3%	49098	57749
	2%	98997	101770
δR	4%	4749	4749
	3%	6436	6436
	2%	11238	11238
	1%	26911	26911

3.4. Effect of detector threshold

This section describes the performance of the model at different detector thresholds. As shown in Fig. 1(a), the coincidence count rate is a function of the detector threshold. The Compton peak ratio varies with the threshold, and the noise level can decrease significantly as the threshold increases. We trained separately for each threshold and then measured the performance of the model using the test dataset reserved for each threshold. The number of coincidences in the training datasets corresponding to each threshold is the same. The number of photopeak coincidences increases with the threshold, but the total number of coincidences in each training dataset remains the same. The prediction accuracy of the model increases as the threshold increases. For the three-energy window

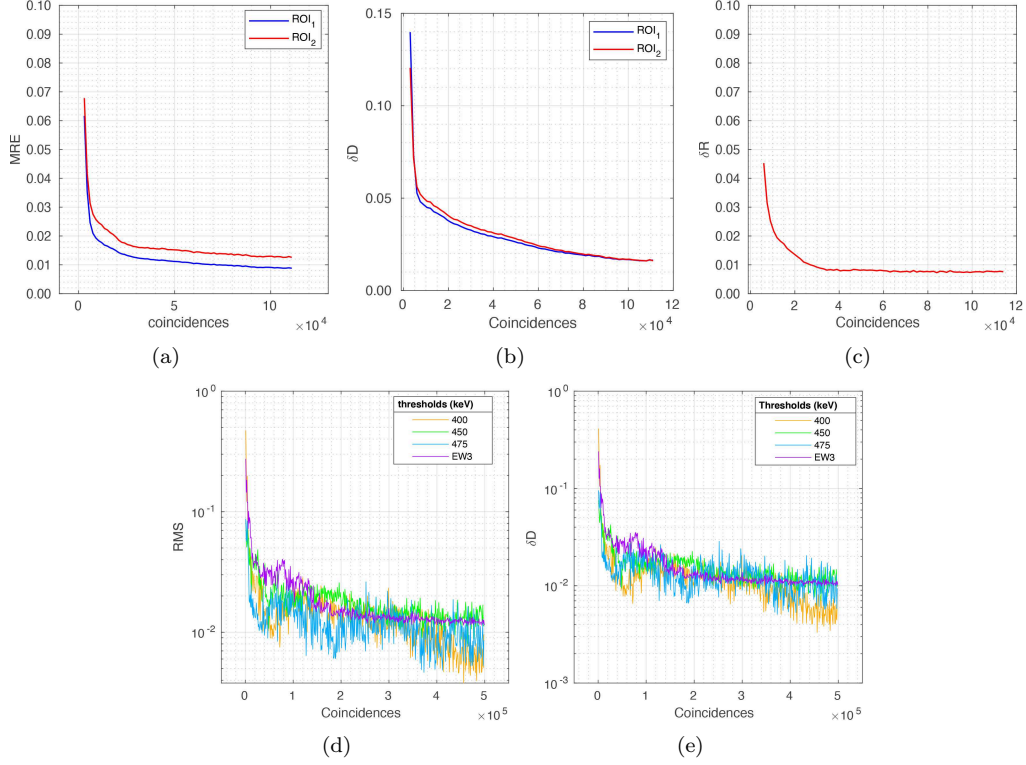


Figure 7. (a). Shows the MRE for ROI₁ and ROI₂ as a function of coincidences, (b) Absolute fractional dose difference for ROI₁ and ROI₂ as a function of coincidence data, (c) shows a fractional shift in the BP as a function of coincidence data, (d) shows the MRE as a function of coincidences for 90 MeV proton beam on \log_{10} scale, and (e) shows the fractional dose difference as a function of coincidences for a 90 MeV proton beam on \log_{10} scale.

(EW3) method, significantly low errors and stable values are observed, as shown in Fig. 8. EW3 dataset includes three energy windows starting at a threshold of 150 KeV, as described in Sec. 2.4.

3.5. Sensitivity consideration

The count-based analysis in Sec. 3.3 shows that the performance of the model improves significantly with more coincidence data. However, our detector prototype encountered low sensitivity, and due to the rectangular geometry of the detector, the absolute sensitivity in the y and z directions along the plane was not the same. We calculated the absolute sensitivity by simulating a point source passing through the centerline in the y and z directions. For our prototype, the absolute sensitivity at the mid-plane of the detector's field of view (FOV) is 0.91%. The off-center sensitivity is normalized to the maximum sensitivity position, which experiences a steep sensitivity loss, as shown in Fig. 9(a). Increasing the area of the detection plan along the y and z directions can improve the sensitivity. The increase in the detected coincidences for different proton energies and four detector sizes are shown in Fig. 9(b). By doubling the area of the base detector prototype, we can increase the detected

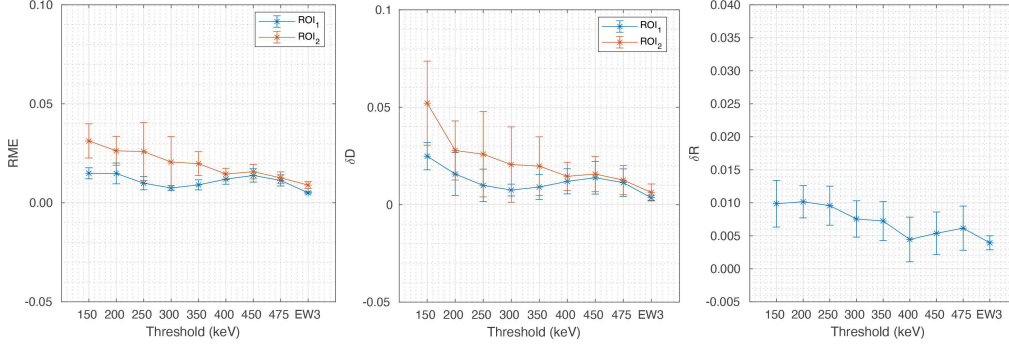


Figure 8. (a) Shows the MRE for ROI₁ and ROI₂ as a function of the threshold of the detector, (b) Absolute fractional dose difference (δD) for ROI₁ and ROI₂ as a function of the threshold of the detector, (c) shows a fractional shift in the BP as a function of threshold.

coincidence by a factor of approximately 3, and by increasing the area by a factor of 4, the number of detected counts can be increased by a factor of 12. To achieve the most stable prediction stage using the EW3 training method, about 10^5 of coincidences are required, as shown in Fig. 7(d). To achieve the 10^5 coincidence, a fourfold increase in detector geometry applies to the extreme case of 30 cm phantom size. Another approach could be used to perform sensitivity correction or introduce some boosting algorithm to encrypt this information in the dataset passed to the deep learning model.

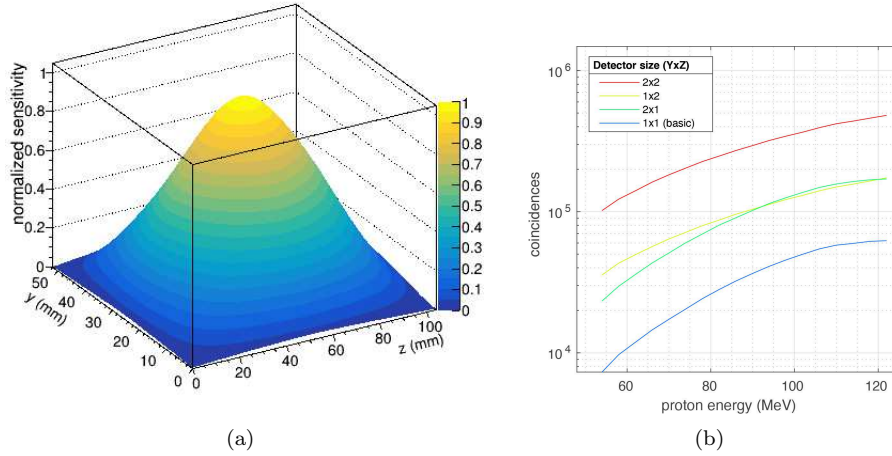


Figure 9. (a) shows the normalized sensitivity of the basic palm-sized PET module for 30 cm phantom case, (b) shows the effect on detected coincidences with increased detector sizes.

4. Discussion

Conditional generative adversarial networks are one of the variants of the GAN model. GAN models help simulate new data with impressive performance, but model convergence and stability are extremely challenging. Mode collapse is another serious problem for GANs models when the generator is not successful enough to produce different data. In our study, mode collapse was avoided using the cGAN variant. The model learns conditional probabilities using auxiliary information rather than random noise vectors from the latent space. Since the BP position is different for each energy, it is shown that the average position of the maximum pixel intensity varies with each energy. Therefore, fortunately, in our study, shifts in BP were very effective in calibrating the mode collapse problem, which converged to less than 1% for our data for different energies, positions, and spot sizes. This strategy provides the model with the most diverse features in the training data. This is also a good preventive measure to eliminate model instability and divergence issues. The study demonstrated the feasibility of directly mapping proton dose from the coincidence domain to the dose domain using raw data. This method can bypass the conventional reconstruction chain and learn features directly from the projection data. Large-size ring PET solutions have been proposed for dose mapping, but our study proposes the use of a small palm-sized PET detector solution leveraging the deep learning framework to optimize for the minimum number of coincidences needed for reconstruction. Our dual-head setup has a geometrically active area 100 times smaller than the PET solution proposed in the previous study (Hu et al. 2020). In Hu *et al.*, there were 88,000 crystals, whereas we have only 1024 crystal elements and a complete detector with 10 times smaller geometric size and 85 times less calibration load.

In our study, we adjusted the relative positions of the phantom and detector such that the phantom is always in the center of the detector along the transverse depth. But the detector is aligned along the beam direction with the phantom edge at the beam entry point. Validation along the beam direction is limited by the size of the 104 mm detector, which can be addressed in two possible ways. One is to map the complete dose profile with a large detector, and the other is to reconstruct only the Bragg peak position as an ROI. The former demands an increase in the geometric efficiency along the beam direction for energies in the proton range above 102 mm, depending on the material density, while the latter requires a robust alignment algorithm that can translate the detector accordingly to focus on BP.

To evaluate the performance of our method, we used more realistic and direct variables called mean relative error per pixel, the fractional difference in absolute dose, and fractional shift in BP. The shift in BP is a geometric feature that shows faster convergence and less uncertainty than the change in absolute dose. This can be seen in Fig. 7(c) and the relationship between counts and the absolute dose difference in Fig. 7(b). BP requires 5 to 9 times fewer coincidence data to converge faster than the data required for the dose to converge to the same level of accuracy. There is a feature threshold after which range shift can be predicted with acceptable accuracy. At the same time, with very low concordance data, we did not get significantly convergent dose curves, which resulted in undefined parts at the beginning of each performance curve, as shown in Fig. 7(a)-(c). The prediction of the absolute dose is still challenging, but looking at the trend in Fig. 7(b), it can be inferred that the accuracy improves with increasing coincidence. Using our detector prototype, the study proposes an estimated number of protons required for dose mapping. According to Table 5, approximately 23,000 coincidences are required to obtain absolute dose uncertainty below 4% for ROI₁, which requires 2.2×10^{10} protons. To reach the 4% prediction uncertainty in the BP position, the model needs only 47,000 photopeak coincidences which are equivalent to 3×10^9 protons. To

approach an absolute dose difference of 2%, approximately 5 times more photopeak coincidences are required, which is equivalent to 10×10^{10} protons. The least the uncertainty, the higher the coincidence, and hence proton flux is required. To achieve the mentioned number of coincidences, the geometric efficiency of the detector, scan time, or proton flux is the active parameters that is sensitive to increase coincidence data. Considering a possible clinical constraint on increasing proton flux beyond a certain limit, optimized geometric efficiency and coincidence data scan time can be more useful for achieving required coincidences. Coincidence data can be increased approximately 3 times by 2 times increase in the detector size. If we increase our detector size 4 times, we can increase the coincidence up to 5 times Fig. 9(b). The detected coincidence rate varies by the diameter of the phantom, making the use of basic palm-sized PET a challenging choice for large FoV. However, it can still be effective for small phantoms where the number of coincidences can increase Fig. 1(b). An increase in detector size, convolution of sensitivity correction, and optimal scan time selection can help to increase coincidences to meet the required coincidences. The model is studied with two training approaches, passing a single condition of the coincidence map to the model and passing three conditions wrapped as three channels of the source image. Using multiple channels in the input condition is a superior approach because it increases the data conditions. Hence, more kernel channels are available for convolution, summed up as a single cross-correlation map. In the case of any potential shift in photopeak, Compton's part of the spectrum would get a feature of photopeak variation, and this feature will be incorporated as a condition in a multi-channel approach. The idea of encrypting energy information as channels was not used before indirect image reconstruction and dose mapping studies. Another advantage of this scheme is the possible elimination of threshold dependence on the model. It is also possible to use the source image to train only on the photopeak coincidences or on the selected threshold. Still, it requires 8 times more photopeak coincidence data to compete with the same level of accuracy, which is achieved using a multi-channel approach. It is possible to introduce more than three energy windows, phantom information, detector response, and time of flight information and consolidate them as input conditions that can be examined in another dedicated study. A major incentive is the ability to map the dose directly from the raw unreconstructed detector output data in less than one second (25 ms) using the trained model. One potential application of our study can be in FLASH therapy, where ultra-high proton doses ($> 30 \text{ Gys}^{-1}$) (Verhaegen et al. 2021) are delivered in a short time window of less than one second where prompt gamma detection may not be realistic. The proposed study is 2D dose mapping, but it can be extended as a 3D study by incorporating the time of flight, the detector's calibration condition, the detector's sensitivity, local crystal efficiency, and phantom information. This study does not account for the washout effect and loss in positron activity during the beam-on time, but it can be incorporated into the subsequent research. Our analysis is straightforward, and with the use of patient CT, simulation of activity profiles for different energies, spot sizes, beam positions, and small PET detector design with detector parameters, e.g., energy resolution, time resolution, detector sensitivity, and crystal detection efficiency bring it nearer to the actual situation.

5. Conclusion

This work demonstrates the potential for 2D dose validation and direct reconstruction using compact palm-sized PET modules by harnessing the potential of cGAN-based deep learning framework. In our study, mean relative error, absolute dose difference, and shift in BP were used as figures of merit. Our method can obtain Bragg peak position results with less than 1% and absolute dose with less than 2% uncertainty achieved with $\sim 10^5$ coincidences when irradiating with mono-energetic

proton beams between 50 MeV and 120 MeV for less than five minutes of acquisition. Our study opens a window to explore the application of deep learning models in dose mapping using small amounts of coincidence data. Including auxiliary information corresponding to the detected photon energy by feeding different conditions related to different set thresholds leads to an improved stability in the predicted output. The fractional dose difference between predicted dose and the true dose distribution improves from 2.6% to 1.6% by providing the additional condition corresponding to the photon energy. In the future we intend to evaluate our model predictions on experimental data using compact detectors. Our model can be a valuable tool for treatment planning and quality assurance in particle therapy.

Acknowledgement

The research and development was funded by the Academia Sinica thematic research program with the project number AS-TP-108-ML0. This work also used ASGC (Academia Sinica Grid-computing Center) Distributed Cloud resources, which is supported by Academia Sinica, Taiwan.

References

- Alessio, A., Sauer, K. & Kinahan, P. (2005), ‘Analytical reconstruction of deconvolved fourier rebinned pet sinograms’, *Physics in medicine & biology* **51**(1), 77.
- Attanasi, F., Knopf, A., Parodi, K., Paganetti, H., Bortfeld, T., Rosso, V. & Guerra, A. D. (2011), ‘Extension and validation of an analytical model for in-vivo pet verification of proton therapy—a phantom and clinical study’, **56**(16), 5079–5098.
URL: <https://doi.org/10.1088/0031-9155/56/16/001>
- Enghardt, W., Parodi, K., Crespo, P., Fiedler, F., Pawelke, J. & Pönisch, F. (2004), ‘Dose quantification from in-beam positron emission tomography’, *Radiotherapy and Oncology* **73**, S96–S98. Carbon-Ion Therapy.
URL: <https://www.sciencedirect.com/science/article/pii/S0167814004800240>
- Fahey, F. H. (2002), ‘Data acquisition in pet imaging’, *Journal of nuclear medicine technology* **30**(2), 39–49.
- Fiedler, F., Shakin, G., Skowron, J., Braess, H., Crespo, P., Kunath, D., Pawelke, J., Pönisch, F. & Enghardt, W. (2010), **55**(7), 1989–1998.
URL: <https://doi.org/10.1088/0031-9155/55/7/013>
- Fourkal, E., Fan, J. & Veltchev, I. (2009), ‘Absolute dose reconstruction in proton therapy using PET imaging modality: feasibility study’, **54**(11), N217–N228.
URL: <https://doi.org/10.1088/0031-9155/54/11/n02>
- Grevillot, L., Bertrand, D., Dessy, F., Freud, N. & Sarrut, D. (2011), ‘A monte carlo pencil beam scanning model for proton treatment plan simulation using GATE/GEANT4’, **56**(16), 5203–5219.
URL: <https://doi.org/10.1088/0031-9155/56/16/008>
- Hu, Z., Li, G., Zhang, X., Ye, K., Lu, J. & Peng, H. (2020), ‘A machine learning framework with anatomical prior for online dose verification using positron emitters and PET in proton therapy’, **65**(18), 185003.
URL: <https://doi.org/10.1088/1361-6560/ab9707>
- Häggström, I., Schmidtlein, C. R., Campanella, G. & Fuchs, T. J. (2019), ‘DeepPET: A deep encoder–decoder network for directly solving the PET image reconstruction inverse problem’, *Medical Image Analysis* **54**, 253–262.
URL: <https://www.sciencedirect.com/science/article/pii/S1361841518305838>
- Iriarte, A., Marabini, R., Matej, S., Sorzano, C. & Lewitt, R. (2016), ‘System models for PET statistical iterative reconstruction: A review’, *Computerized Medical Imaging and Graphics* **48**, 30–48.
URL: <https://www.sciencedirect.com/science/article/pii/S0895611115001901>
- Isola, P., Zhu, J.-Y., Zhou, T. & Efros, A. A. (2017), ‘Image-to-image translation with conditional adversarial networks’, *2017 IEEE Conference on Computer Vision and Pattern Recognition (CVPR)* pp. 5967–5976.
- Jan, S., Benoît, D., Becheva, E., Carlier, T., Cassol, F., Descourt, P., Frisson, T., Grevillot, L., Guigues, L., Maigne, L., Morel, C., Perrot, Y., Rehfeld, N., Sarrut, D., Schaart, D. R., Stute, S., Pietrzyk, U., Visvikis, D., Zahra, N. & Buvat, I. (2011), ‘GATE v6: a major enhancement of the GATE simulation platform enabling modelling of CT and radiotherapy’, **56**(4), 881–901.
URL: <https://doi.org/10.1088/0031-9155/56/4/001>

- Liu, C., Li, Z., Hu, W., Xing, L. & Peng, H. (2019), ‘Range and dose verification in proton therapy using proton-induced positron emitters and recurrent neural networks (RNNs)’, **64**(17), 175009.
URL: <https://doi.org/10.1088/1361-6560/ab3564>
- Lu, H.-M. (2008), ‘A potential method for in vivo range verification in proton therapy treatment’, *Physics in Medicine & Biology* **53**(5), 1413.
- Masuda, T., Nishio, T., Kataoka, J., Arimoto, M., Sano, A. & Karasawa, K. (2019), ‘ML-EM algorithm for dose estimation using PET in proton therapy’, **64**(17), 175011.
URL: <https://doi.org/10.1088/1361-6560/ab3276>
- Min, C.-H., Kim, C. H., Youn, M.-Y. & Kim, J.-W. (2006), ‘Prompt gamma measurements for locating the dose falloff region in the proton therapy’, *Applied physics letters* **89**(18), 183517.
- Mirza, M. & Osindero, S. (2014), ‘Conditional generative adversarial nets’, *arXiv preprint arXiv:1411.1784*.
- Nemallapudi, M. V., Rahman, A., Chen, A. E.-F., Lee, S.-C., Lin, C.-H., Chu, M.-L. & Chou, C.-Y. (2021), ‘Positron emitter depth distribution in pmma irradiated with 130 mev protons measured using tof-pet detectors.’, *IEEE Transactions on Radiation and Plasma Medical Sciences* pp. 1–1.
- Oussidi, A. & Elhassouny, A. (2018), Deep generative models: Survey, in ‘2018 International Conference on Intelligent Systems and Computer Vision (ISCV)’, IEEE, pp. 1–8.
- Ozoemelum, I., Van der Graaf, E., Van Goethem, M.-J., Kapusta, M., Zhang, N., Brandenburg, S. & Dendooven, P. (2020), ‘Feasibility of quasi-prompt pet-based range verification in proton therapy’, *Physics in Medicine & Biology* **65**(24), 245013.
- Paans, A. & Schippers, J. (1993), ‘Proton therapy in combination with pet as monitor: a feasibility study’, *IEEE Transactions on Nuclear Science* **40**(4), 1041–1044.
- Paganetti, H. (2012), ‘Range uncertainties in proton therapy and the role of monte carlo simulations’, **57**(11), R99–R117.
URL: <https://doi.org/10.1088/0031-9155/57/11/r99>
- Paganetti, H. & El Fakhri, G. (2015), ‘Monitoring proton therapy with pet’, *The British journal of radiology* **88**(1051), 20150173.
- Parodi, K. (2000), ‘Potential application of PET in quality assurance of proton therapy’, **45**(11), N151–N156.
URL: <https://doi.org/10.1088/0031-9155/45/11/403>
- Parodi, K. & Bortfeld, T. (2006), ‘A filtering approach based on gaussian–powerlaw convolutions for local PET verification of proton radiotherapy’, **51**(8), 1991–2009.
URL: <https://doi.org/10.1088/0031-9155/51/8/003>
- Parodi, K., Paganetti, H., Shih, H. A., Michaud, S., Loeffler, J. S., DeLaney, T. F., Liebsch, N. J., Munzenrider, J. E., Fischman, A. J., Knopf, A. & Bortfeld, T. (2007), ‘Patient study of in vivo verification of beam delivery and range, using positron emission tomography and computed tomography imaging after proton therapy’, *International Journal of Radiation Oncology Biology Physics* **68**(3), 920–934.
URL: <https://www.sciencedirect.com/science/article/pii/S036030160700377X>
- Remmele, S., Hesser, J., Paganetti, H. & Bortfeld, T. (2011), ‘A deconvolution approach for PET-based dose reconstruction in proton radiotherapy’, **56**(23), 7601–7619.
URL: <https://doi.org/10.1088/0031-9155/56/23/017>

- Ronneberger, O. & Fischer, Philipp and Brox, T. (2015), U-net: Convolutional networks for biomedical image segmentation, *in* N. Navab, J. Hornegger, W. M. Wells & A. F. Frangi, eds, ‘Medical Image Computing and Computer-Assisted Intervention – MICCAI 2015’, Springer International Publishing, Cham, pp. 234–241.
- Schneider, W., Bortfeld, T. & Schlegel, W. (2000), ‘Correlation between CT numbers and tissue parameters needed for monte carlo simulations of clinical dose distributions’, **45**(2), 459–478.
URL: <https://doi.org/10.1088/0031-9155/45/2/314>
- Su, Z., Hsi, W., Forthomme, J. & Rossomme, S. (2020), ‘Evaluations of a flat-panel based compact daily quality assurance device for proton pencil beam scanning (pbs) system’, *Physica Medica* **80**, 243–250.
- Tong, S., Alessio, A. M. & Kinahan, P. E. (2010), ‘Image reconstruction for pet/ct scanners: past achievements and future challenges’, *Imaging in medicine* **2**(5), 529–545.
- Vaquero, J. J. & Kinahan, P. (2015), ‘Positron emission tomography: Current challenges and opportunities for technological advances in clinical and preclinical imaging systems’, *Annual Review of Biomedical Engineering* **17**(1), 385–414. PMID: 26643024.
URL: <https://doi.org/10.1146/annurev-bioeng-071114-040723>
- Verhaegen, F., Wanders, R.-G., Wolfs, C. & Eekers, D. (2021), ‘Considerations for shoot-through flash proton therapy’, *Physics in Medicine & Biology* **66**(6), 06NT01.
- Watts, D. A., Amaldi, U., Go, A., Hajdas, W., Iliescu, S., Malakhov, N., Samarati, J., Sauli, F. et al. (2009), A proton range telescope for quality assurance in hadrontherapy, *in* ‘2009 IEEE Nuclear Science Symposium Conference Record (NSS/MIC)’, IEEE, pp. 4163–4166.
- Winterhalter, C., Taylor, M., Boersma, D., Elia, A., Guatelli, S., Mackay, R., Kirkby, K., Maigne, L., Ivanchenko, V., Resch, A. F. et al. (2020), ‘Evaluation of gate-rtion (gate/geant4) monte carlo simulation settings for proton pencil beam scanning quality assurance’, *Medical Physics* **47**(11), 5817–5828.
- Zhang, X., Hu, Z., Zhang, G., Zhuang, Y., Wang, Y. & Peng, H. (2021), ‘Dose calculation in proton therapy using a discovery cross-domain generative adversarial network (discogan)’, *Medical Physics* **48**(5), 2646–2660.